Characterising and predicting the relationship between translaminar fracture toughness and pull-out length distributions under distinct temperatures

B. Yu[1,2], T. J. Katafiasz[1], S. Nguyen[1], G. Allegri[3], J. Finlayson[4], E. S. Greenhalgh[1], S. T. Pinho [1], S. Pimenta[2*]

[1] Department of Aeronautics, Imperial College London, South Kensington Campus, SW7 2AZ London, United Kingdom
[2] Department of Mechanical Engineering, Imperial College London, South Kensington Campus, SW7 2AZ London, United Kingdom
[3] Bristol Composites Institute (ACCIS), University of Bristol, Queen's Building, Bristol, BS8 1TR, UK
[4] Structural Systems Design, Rolls-Royce plc, Derby, UK

Abstract

The translaminar fracture toughness reflects the damage tolerance of a fibre-reinforced composite under longitudinal tension, which often governs final failure of structures. One of the main energy-dissipation mechanisms that contributes to the translaminar toughness of composites is the fibre pull-out process. The present study aims to quantify and model the statistical distribution of fibre pull-out lengths formed on the translaminar fracture surface of composites, for the first time in the literature; this is done under different temperatures, so that the relationship between pull-out length distributions, micromechanical properties, and the translaminar fracture toughness can be established. The fracture surfaces of cross-ply compact-tension specimens tested under three different temperatures have been scanned through X-ray computed tomography to quantify the extent of fibre pull-out on the fracture surfaces; the distribution of pull-out lengths showed a larger average and larger variability with an increase in temperature, which also lead to an increase in translaminar fracture toughness. A similar trend has been captured by the proposed analytical model, which predicts the pull-out length distribution based on the analysis of quasi-fractal idealisations of the fracture surface, yielding an overall accuracy of more than 85%.

Yu B, Katafiasz TJ, Nguyen S, Allegri G, Finlayson J, Greenhalgh ES, Pinho ST, Pimenta S., "**Characterizing and predicting the relationship between translaminar fracture toughness and pull-out length distributions under distinct temperatures**", *Phil. Trans. R. Soc. A* 380 (2022), 20210220. DOI: 10.1098/rsta.2021.0220.

Nomenclature

Symbol	*Description*
c	Coordination number
i	Hierarchical level
h_{po}	Pull-out height
l_{po}	Pull-out length
$\mathcal{F}_{\mathrm{po}}$	Cumulative distribution function (CDF) for pull-out length
$G_{\mathrm{Ic}}^{\mathrm{lam}}$	Laminate-level translaminar propagation fracture toughness
G_{Ic}^{0}	Ply-level translaminar propagation fracture toughness
G_{IIc}	Mode II fracture toughness
$\mathcal{H}_{\mathrm{po}}$	Stochastic pull-out height
$\mathcal{L}_{\mathrm{po}}$	Stochastic pull-out length
τ_{SL}	Shear strength (yield stress)
τ_{μ}	Pull-out frictional stress
$\xi^{[i]}$	A binary variable indicating whether or not the hierarchical level i contributes to the pull-out height of the particular fibre analysed
Ξ	The combination defining a pull-out height, i.e. the set of binary variables $\left[\xi^{[i^{\max}]}, \xi^{[i^{\max}-1]}, \dots, \xi^{[1]}, \xi^{[0]}\right]$ for each fibre
k	The number of hierarchical levels contributing to the pull-out height in a given combination
$\nu_{[k]}$	The frequency of each individual k −combination
$\eta^{[i]}$	The number of times that the pull-out length distribution of an individual level i needs to be sampled for random pull-out lengths

1 Introduction

Carbon fibre reinforced polymer (CFRP) materials have found increasing applications in primary aircraft components. One of the major design considerations is to address the durability and damage tolerance requirements to avoid catastrophic failure. Significant efforts have been focused on the characterisation of the translaminar fracture toughness of composites (i.e. to break the material across the fibres), as this property is a quantitative measure of the damage tolerance of fibre-reinforced composites under longitudinal tension [1-6].

The translaminar fracture toughness of a unidirectional continuous-fibre composite depends on constituent properties, especially on the fibre/matrix interface properties. It has been recognised that the fracture energy is dissipated by two dominant mechanisms, namely fibre/matrix interfacial debonding (corresponding to a debonding component of the work of fracture, W_{deb}) and post-debonding pull-out of fibres and bundles (corresponding to a pull-out component of the work of fracture, W_{po}) [7]. The latter is strongly related to the pull-out lengths (l_{po}) developed during the fracture process:

$$W_{\mathrm{po}} = \frac{1}{2} \cdot C \cdot \tau_{\mu} \cdot {l_{\mathrm{po}}}^{2} , \tag{1}$$

where C is the perimeter of debonded fibres or bundles, and the in-situ frictional stress τ_{μ} provides resistance to pull-out.

Fractographic studies of fracture surfaces have been carried out to observe the crack path in translaminar fracture, inspect the bonding quality of fibre/matrix interfaces, and observe the degree of fibre pull-out [3-6]. It has been noted that the translaminar fracture surface of CFRPs features a statistical distribution of pull-outs across a range of scales, ranging from individual fibres to large bundles [1, 8, 9]. These observations were mainly performed by conventional 2D imaging techniques such as optical microscopy and scanning electron microscopy (SEM). However, pull-out length distributions have never been quantified experimentally.

In comparison to conventional 2D imaging techniques, X-ray computed tomography (xCT) offers an advantage: it provides an accurate 3D representation of the material, which enables an increasing level of information to be extracted compared to that of a 2D image [10, 11]. There are many applications of xCT to the study of composites. In some cases, it has allowed a range of measurements of internal microstructures, such as fibre orientation, manufacturing defects and extent of damage [12-14]. In other cases, it has been used for monitoring the evolution of features of interest (e.g. damage) over time via time-lapse experiments [15]. Therefore, it can be anticipated that xCT is well suited for the quantitative analysis of fibre pull-out length distributions, although this has never been done.

Several statistical micromechanical models have been proposed to predict the fracture toughness of unidirectional continuous-fibre composites through the prediction of pull-out lengths. Most of these models [8, 16, 17] focus on predicting the pull-out length distribution of fibres or bundles, by taking into account the stress distribution on debonded fibres and the failure probability at given pull-out length; however, these models considered that the pull-out process occurred at a single scale (i.e. that of the fibres or that of experimentally-observed bundles), meaning that size effects associated with the pull-out features observed across the scales were often overlooked. These size effects have been addressed in Pimenta and Pinho's model [9] which describes the translaminar fracture surface as a self-affine hierarchy formed by pull-out of individual fibres and bundles. In this model, the debonding and pull-out length distributions are derived as a function of fibre/bundle tensile strength distribution and interfacial properties. This has led to successfully predicting the translaminar fracture toughness for a wide range of material systems, and under different environmental conditions

(including different temperatures and moisture levels) [5]; however, the pull-out length distributions predicted by the model have never been validated experimentally.

Previous studies have shown that the translaminar fracture toughness of composites increases with increasing temperature, and that this increase is accompanied by an apparent (observed qualitatively) increase in fibre pull-out [4,5]; however, the effect of temperature on pull-out length distributions has never been quantified. Such quantification could potentially result in two benefits: (i) revealing the relationship between pull-out processes (i.e. an underlying damage mechanism on a microscopic level) and fracture toughness (i.e. a macroscopic property of the composite); (ii) gaining useful insights into the response of composites to varying temperatures, which would inform the design of composite materials and structures for use in different service environments.

Therefore, the objective of this study is to provide a comprehensive investigation into the relationship between translaminar fracture toughness and pull-out length distributions under different temperatures, based on experimental characterisation and model prediction.

2 Materials and mechanical testing

2.1.1 Specimen manufacture

All composite panels were fabricated from M21/AS7 prepreg with a layup of $[(90/0)_8/90/(0/90)_8]$, and subsequently cured in an autoclave according to the supplier's recommended curing cycle [18].

2.1.2 Compact tension tests

Compact tension tests were carried out with a loading speed of 0.5 mm/min at three different temperatures, i.e. -55°C, 23°C and 90°C to characterise the translaminar fracture toughness $G_{\mathrm{Ic}}^{\mathrm{lam}}$ following the test method in [1]. For each temperature, four tests were carried out.

2.1.3 Data reduction

The *R*-curves of translaminar fracture toughness for each temperature were obtained via a data reduction technique based on the compliance calibration method [2]. The optically-measured crack length a and the corresponding compliance C^{exp} (determined from the load-displacement curve) were fitted with the following expression:

$$C^{\mathrm{exp}} = (\alpha a + \beta)^{\chi} . \tag{2}$$

The unknown constant parameters α, β and χ were estimated by a least squares regression. The translaminar fracture toughness of the laminate $G_{\mathrm{Ic}}^{\mathrm{lam}}$ was subsequently calculated as a function of the crack length:

$$G_{\mathrm{Ic}}^{\mathrm{lam}}(a) = \frac{P_{\mathrm{c}}^2}{2t^{\mathrm{lam}}} \frac{\mathrm{d}C^{\mathrm{exp}}}{\mathrm{d}a}, \tag{3}$$

where P_{c} is the load corresponding to crack propagation and t^{lam} is the laminate thickness. Assuming the interactions between the different layers are negligible, the translaminar fracture toughness of a laminate was related to that of the individual plies by the rule of mixtures (assuming that the intralaminar toughness in a 90° ply (dominated by matrix-cracking and/or interfacial failure) is negligible compared to the toughness of the 0° ply G_{Ic}^{0}):

$$G_{\mathrm{Ic}}^{0}(a) = \frac{t^{\mathrm{lam}}}{t^{0}} G_{\mathrm{Ic}}^{\mathrm{lam}}(a). \tag{4}$$

3 X-ray computed tomography data acquisition and image processing

3.1 X-ray image acquisition

A simple visual inspection of the photographs in Figure 1 shows that the fracture surfaces of the compact tension specimens consist of a collection of pulled-out fibres and bundles whose lengths cover multiple length scales. In order to quantify these lengths, xCT scans were carried out to achieve a 3D fractographic examination of the fracture surfaces of the compact tension specimens. To prepare for the xCT scans, a small specimen with 10 × 10 mm^2 in the xy plane and full thickness was cut out from one compact tension specimen under each temperature. The cut-out xCT specimen was centred around the initial 5 mm crack region so as to avoid creating any additional damage to the fracture surface. The quantitative analysis of the pull-out length development using xCT data will be discussed in the following sections.

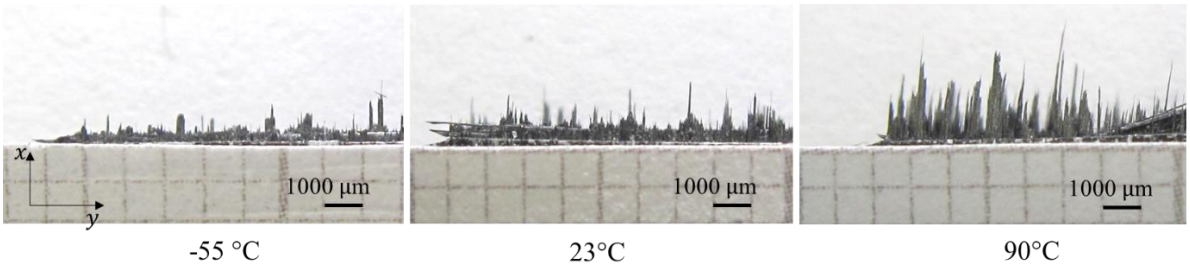

Figure 1: Photographs of fracture surfaces obtained through compact tension tests under different temperatures.

Three fracture surfaces obtained at the three different testing temperatures were xCT scanned on a Zeiss Xradia Versa 620 X-ray microscope, with an accelerating voltage of 80 kV and power of 10 W. A total of 3142 projections were taken as the specimen was rotated over 360° around the longitudinal directional of the specimen (x-direction in Figure 1) in equal increments. The exposure time was 4 s. These projections were collected on the 2k × 2k, 16-bit high-resolution CCD detector. A resolution of 2.5 μm was used, which was adequate to resolve the pull-out of individual fibres with a diameter of 7 μm. This setup resulted in a scan volume having a circular cross section in the yz plane with approximately 5 mm in diameter (which is broadly aligned with the fracture plane), and 5 mm along the x-direction (see Figure 2). Consequently, each scanned fracture surface included more than 150,000 fibres.

The projections were reconstructed into 3D greyscale images (as shown in Figure 2 (a)) using Zeiss XM Reconstructor. The alignment of the 3D xCT image (i.e. with the x-direction perfectly aligned with the pull-out direction) was ensured by tilting the 3D volume in the pre-processing stage. An objective quantification of pull-out length distributions from these X-ray images requires overcoming two challenges:

(i) segmenting the 0° plies (in which fibre pull-out occurs) from the surrounding 90° plies. This segmentation is particularly critical because the length of fibre pull-outs in a 0° ply tends to be smaller near the interfaces with the neighbouring 90° plies than at the mid-thickness of the ply [1, 9]. Therefore, the segmentation should include the entirety of the 0° plies to avoid biasing the pull-out length distributions towards the longer pull-outs that develop mid-thickness, but exclude the 90° plies completely (as these would artificially contribute with (quasi) zero pull-out lengths). Unfortunately, it is not possible to separate 0° and 90° plies simply

bymanual cropping or automatic thresholding operations, due to the similar xCT contrast and similar surface morphology of the 0° and 90° plies (especially at their interfaces).

(ii) establishing a datum plane where fibre pull-out lengths can be assumed zero, which provides a reference for measuring the relative pull-out lengths in 0° plies. This is complicated by the stochastic and hierarchical nature of the fracture surface, whose position along the longitudinal direction (x-direction in Figure 2) oscillates due to (i) pull-out of individual fibres and bundles within each 0° ply, and (ii) uneven transverse fracture planes amongst all 90° plies.

3.2 Quantification of pull-out distributions

This section proposes a systematic methodology to overcome the challenges identified in the previous section and objectively quantify the pull-out distributions on fracture surfaces. This methodology is illustrated in Figure 2, taking the fracture surface of a specimen tested at room temperature as an example, and it includes the following steps:

(i) *3D greyscale data* (see Figure 2 (a)). This 3D data is a map of the X-ray attenuation within the scanned volume. While there is striking contrast between composite (in light grey) and the air (in dark grey), the greyscale intensity is relatively uniform within the composite as a result of (i) similar X-ray attenuation coefficients in fibre and matrix regions and (ii) a relatively low spatial resolution.

(ii) *3D binary image* (Figure 2 (b)). A binary image was obtained by thresholding the *3D greyscale data*. This binary image is essentially a 3D matrix with the entries being set to 0 and 1 for the pixels above and below the fracture surface respectively (note that, below the fracture surface both matrix and fibres are represented by 1).

(iii) *Fracture surface height plot*. A surface plot (Figure 2 (c)) is created by summing all entries of the *3D binary image* along the x-direction and multiplying the result by the pixel size (2.5 μm); it displays the height of each point of the fracture surface, measured from the bottom surface of the scanned volume. The 2D projection of the fracture surface (Figure 2 (d)) reveals that surface heights are distributed almost uniformly within each 90° ply (which corresponds to intralaminar fracture), and significantly vary within each 0° ply (due to the formation of pull-outs; a full statistical analysis of this variability is shown in the Results, particularly Figures 11 and 12).

(iv) *Clustered fracture surface image*: Superpixels (see Figure 14) were generated by clustering pixels on the *2D projection of the fracture surface* (Figure 2 (d)), based on the similarities of pixels in grayscale value and distance. This step was done by passing the *fracture surface height plot* into the Matlab built-in function 'superpixels', which uses the Simple Linear Iterative Clustering (SLIC) algorithm [19].

(v) *Segmented 90° plies image*: A logical mask (see Figure 14) was manually initialised to roughly mark the region of the 90° plies. The mask image was used in conjunction with the *clustered fracture surface* (generated in step (iv)) and the *2D projected fracture surface* (Figure 2 (d), from step (iii)). By executing the Matlab built-in function 'grabcut', the 90° plies were segmented from the original image through an iterative automatic process (known as the GrabCut algorithm) [20], resulting in the *segmented 90° plies image* as shown in Figure 2 (e) and (f), and the complementary *segmented 0° plies image*. At this stage, the segmented 0° and 90° plies should have similar thickness (which is a good high-level check).

(vi) Artefact removal. The *segmented 90° plies image* (Figure 2 (e)) has some large spikes close to the boundary between 0° and 90° plies, which indicates that they were wrongly segmented (i.e. they actually belong to the 0° plies, which was confirmed by visual inspection). Therefore morphological opening and closing [21] were performed with a linear structural element, which largely removed the noise whilst preserving the boundary of the 90° plies; the resulting *corrected segmented 90° plies image* is displayed in Figure 2 (g) and (h).

(vii) Datum-height of individual 90° plies. The datum height of the fracture surface of each segmented 90° ply was determined by averaging the grayscale value of all corresponding pixels in the *corrected segmented 90° plies image*.

(viii) *Fibre pull-out heights map*. For each 0° ply, the average height of its two neighbouring 90° plies (in the *corrected segmented 90° plies image*) was defined as the reference datum for that 0° ply. The height of each pixel in the 0° ply (from the *segmented 0° plies image*) was then offset from this datum, which resulted in the relative *pull-out height map* of all fibres in each 0° ply, shown in Figure 2 (i) and (j).

(ix) Statistical distribution of fibre pull-outs. Having applied the steps above, a histogram can now be plotted to reveal the statistical distribution of the absolute value of fibre pull-out heights for all 0° plies in the scanned volume (results will be shown in Section 5). This distribution characterises objectively the amount of pull-out in the translaminar fracture surface.

At this point, we note that the pull-out distributions determined using this methodology represent the distance between the fracture surface of individual fibres and an average fracture plane of the corresponding ply – hereafter named "pull-out height". Due to the hierarchical nature of a translaminar fracture surface (where an individual fibre protrudes from its neighbours within a small bundle, and that small bundle itself may protrude from its neighbours within a larger bundle), this pull-out height is different from the length over which individual fibres or bundles protrude from their neighbours in the fracture surface; the latter is commonly referred to as "pull-out length". This difference between pull-out *heights* and pull-out *lengths* will be further explored in the model development presented next, and illustrated in Figure 4.

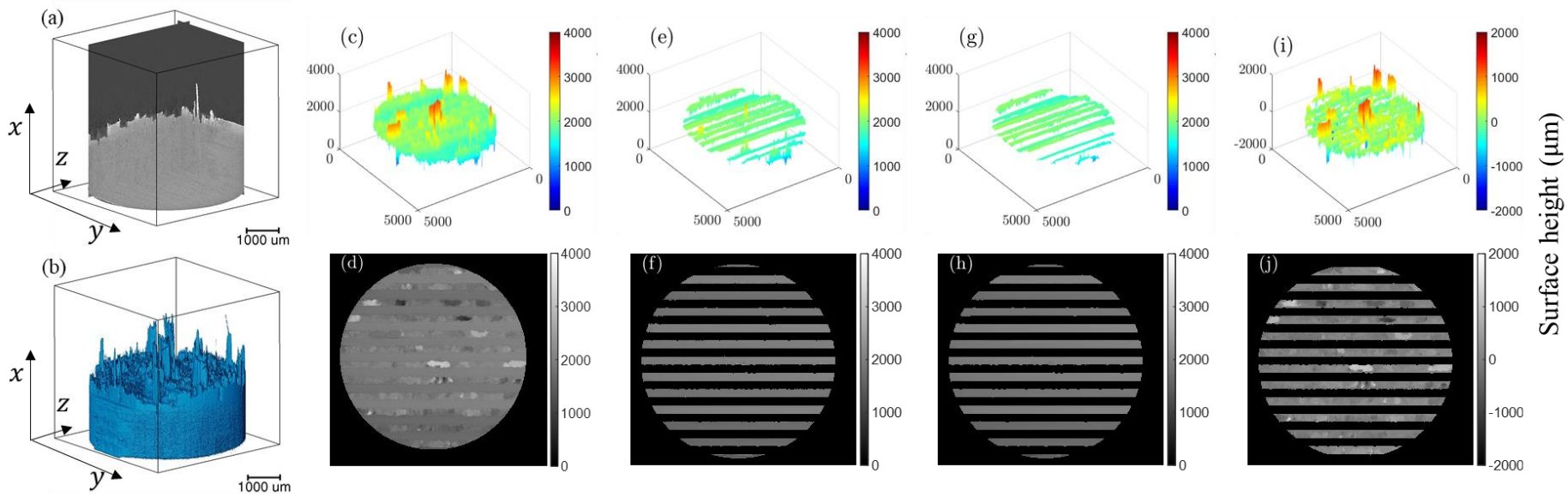

Figure 2: An illustrative workflow showing (a) virtual orthoslices, (b) 3D binary image, (c) fracture surface consisting of both 0° and 90° plies, (d) 2D projection of fracture surface, (e) the segmented 90° plies after applying the graph cut algorithm, (f) 2D projection of (e), (g) smoothed 90° plies after performing the morphological operations, (h) 2D projection of (g), (i) the segmented 0° plies after calibration, and (j) 2D projection of (i). (All dimensions in µm)

4 Model development to predict pull-out distributions

4.1 Model background

In this section, a brief description of the statistical micromechanical model for the fracture toughness of FRPs proposed by Pimenta and Pinho [9] is presented, upon which the present study is built. Detailed mathematical derivations and stress analyses can be found in the original paper [9].

Pimenta and Pinho established an analytical model to predict the translaminar fracture toughness with two underlying assumptions [9]: (i) the translaminar fracture surface of a composite is developed in a hierarchical failure process, where individual fibres and bundles fracture discretely at each hierarchical level (or scale); (ii) the fracture surface has a quasi-fractal geometry i.e. repeating the same pattern of pull-out features across multiple scales (or levels). These assumptions are supported by the experimental evidence found in previous fractographic observations [1, 22].

Following the assumptions mentioned above, Figure 3 illustrates a schematic representation of a multi-level fracture surface; each level $[i]$ is a bundle that consists of a constant number of level-$[i-1]$ sub-bundles (or individual fibres, if $i = 1$), of which one is pulled-out from the fracture plane defined by its neighbours. The constant number of sub-bundles in a bundle corresponds to the coordination number c [9], which can depend on the fibre packing: for instance, $c = 7$ for hexagonal and $c = 9$ for square regular packings, as shown in Figure 3; in a real composite with random fibre packing, c is considered as a mathematical parameter, and Pimenta and Pinho showed that the fracture toughness predicted by their model converged for $6 \leq c \leq 9$ [9].

In the quasi-fractal fracture surfaces idealised by Pimenta and Pinho, for each hierarchical level $[i]$, only the central bundle or fibre is significantly protruded from the plane formed by its $c-1$ co-planar neighbours. This gives rise to a distinct pull-out length, which is the distance between the fracture surface of the protruded fibre/bundle and that of the remaining $(c-1)$ neighbours, as shown in Figure 3. For each hierarchical level, this pull-out length, $\mathcal{L}_{\mathrm{po}}^{[i]}$, is a stochastic variable whose Cumulative Distribution Function (CDF) is calculated by Pimenta and Pinho's model, and expressed as follows:

$$\mathcal{F}_{\mathrm{po}}^{[i]}\left(l_{\mathrm{po}}^{[i]}\right) = \Pr\left(\mathcal{L}_{\mathrm{po}}^{[i]} \leq l_{\mathrm{po}}^{[i]}\right). \tag{5}$$

Pull-out length distributions were derived [9] by combining (i) a detailed analysis of the stress field on a generic level-$[i]$ bundle prior to pull-out with (ii) statistical bundle strength distributions calculated through a hierarchical scaling law [23]. In their original model, Pimenta and Pinho then use the CDF of pull-out lengths to calculate an average pull-out length for each hierarchical level, from which they estimate the frictional energy dissipated during the pull-out process, based on Eq. 1. The overall translaminar fracture toughness of the composite is then obtained by summing the contributions from pulling-out fibres and bundles at all hierarchical levels in the fracture surface, as well as the contributions of energy dissipated through debonding (which depends on the mode-II interfacial toughness G_{IIc}) of those fibres and bundles [9]. See Table 1 for all the inputs required by the model.

A key feature of Pimenta and Pinho's translaminar toughness model is the fact that it can predict experimentally-observed size effects, i.e. an increase in translaminar fracture toughness with increasing ply thickness [17]. This is because distinct ply thicknesses will have distinct numbers of fibres across the ply, therefore leading to distinct numbers of hierarchical levels on the fracture surface. Assuming a square packing of fibres (as shown in Figure 3 (b)) with a diameter ϕ^{f} and fibre volume fraction V^{f}, the maximum hierarchical level present in a ply of thickness t^{ply} is estimated as

$$i^{\max} = \log_c \left[\frac{\left(t^{\mathrm{ply}}\right)^2}{\frac{\pi \cdot (\phi^{\mathrm{f}})^2}{4 \cdot V^{\mathrm{f}}}} \right]. \tag{6}$$

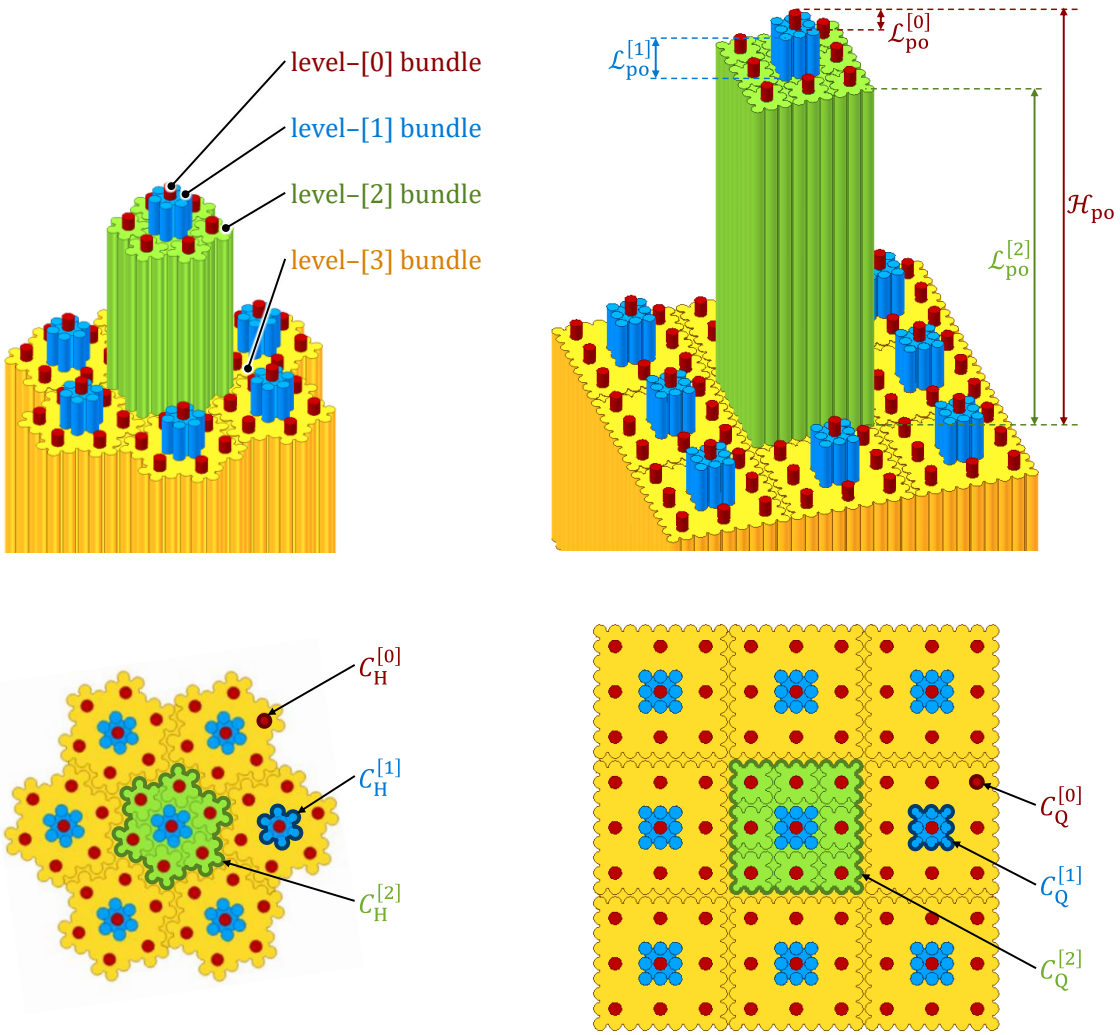

(a) Hexagonal fibre packing with $c = 7$.

(b) Square fibre packing with $c = 9$. The pull-out height shown corresponds to the red fibre with the fracture surface furthest away from the yellow datum surface, i.e. with $\mathcal{H}_{\mathrm{po}} = \mathcal{L}_{\mathrm{po}}^{[0]} + \mathcal{L}_{\mathrm{po}}^{[1]} + \mathcal{L}_{\mathrm{po}}^{[2]}$

Figure 3: Quasi-fractal idealisations of translaminar fracture surfaces [9].

Table 1: Properties of the fibre and interface (model inputs) used in this study

	Property	Model input		
Geometrical	Fibre diameter ϕ^{f} (μm)	7 [24]		
	Fibre volume fraction V^{f} (%)	58.9 [18]		
	Cured ply thickness t^{ply} (mm)	0.184 [18]		
Weibull strength parameters	Scale parameter σ_0^{f}(GPa)	4.43 [5]		
	Shape parameter m	3.65 [5]		
	Gauge length l_{r} (mm)	30 [5]		
Interfacial	Temperature	23°C	-55°C	90°C
	Nominal frictional pull-out stress τ_μ^0 (MPa)	10.0 [9, 25]	15.0[a]	5.7[a]
	Interfacial shear strength τ_{SL} (MPa)	109.0 [18]	140.7[b]	76.8[b]
	Mode II fracture toughness G_{IIc} (kJ/m^2)	100%[c]	130%[c]	67%[c]

[a] τ_μ^0 for -55°C and 90°C were predicted based on the analytical solution provided in [5], which accounts for the effect of temperature on the interfacial pressure (due to different coefficients of thermal expansion of the fibre and matrix).

[b] τ_{SL} for -55°C and 90°C were estimated assuming the same proportional effect of temperature on the experimentally determined shear strength as reported in [5].

[c] G_{IIc} was measured in [5] for a similar type of aerospace-grade composite material. Due to the commercial sensitivity of the material used in [5], a normalised G_{IIc} was used here.

4.2 Methodology for predicting pull-out distributions

4.2.1 Challenges and strategy

The idealised hierarchical fracture surface of a single 0° ply embedded in a laminate (as in the compact tension specimens tested experimentally) is formed by fibres broken at different heights. For each fibre on the fracture surface, the total pull-out height is the combination of stochastic pull-out lengths from several hierarchical levels, as exemplified in Figure 4. Predicting the pull-out height distribution of this stochastic hierarchical fracture requires overcoming the following challenges, which will be done over the subsequent subsections:

(i) Systematically identifying the relationship between stochastic pull-out heights and the pull-out lengths at the different hierarchical levels, for any value of c and $i^{\max}$;
(ii) Obtaining stochastic distributions of the pull-out lengths at the different hierarchical levels present in the fracture surface (i.e. $\mathcal{L}_{\mathrm{po}}^{[0]}$, $\mathcal{L}_{\mathrm{po}}^{[1]}$, … $\mathcal{L}_{\mathrm{po}}^{[i^{\max}-1]}$, $\mathcal{L}_{\mathrm{po}}^{[i^{\max}]}$);
(iii) Defining a generic algorithm to compute stochastic distributions of pull-out heights in a computationally efficient way.

4.2.2 Relationship between pull-out heights and pull-out lengths

To address the first challenge, let us analyse a fracture surface of level $i^{\max} = 3$ and coordination number $c = 9$, as shown in Figure 4. For this particular case, Figure 4 defines the

relationship between (i) the pull-out height ($\mathcal{H}_{\mathrm{po}}$) of every fibre in the fracture surface and (ii) the pull-out lengths of the individual levels which are present in the fracture surface (i.e. $\mathcal{L}_{\mathrm{po}}^{[0]}$, $\mathcal{L}_{\mathrm{po}}^{[1]}$, $\mathcal{L}_{\mathrm{po}}^{[2]}$, and $\mathcal{L}_{\mathrm{po}}^{[3]}$). Using this particular case as a supporting example, we will now generalise the relationship between $\mathcal{H}_{\mathrm{po}}$ and $\mathcal{L}_{\mathrm{po}}^{[i]}$ for a generic case.

For each fibre on a fracture surface, its pull-out height $\mathcal{H}_{\mathrm{po}}$ results from a combination of pull-out lengths of different hierarchical levels; it is then useful to identify whether a given hierarchical level $0 \leq i \leq i^{\max}$ contributes or not to the pull-out height of a particular fibre. This identification can be done by defining a binary variable $\xi^{[i]}$: if $\xi^{[i]} = 1$, then the hierarchical level i contributes to the pull-out height of the particular fibre analysed; if $\xi^{[i]} = 0$, it does not. Therefore, each pull-out height is characterised by a set of $i^{\max} + 1$ binary variables $\xi^{[i]}$, with $i = \{1, 2, \dots, i^{\max} - 1, i^{\max}\}$. This allows us to define a relationship between pull-out height and pull-out lengths, valid for every fibre on the fracture surface regardless of which hierarchical levels contribute to its pull-out height, as follows:

$$\begin{aligned}\mathcal{H}_{\mathrm{po}}^{\left[\xi^{[i^{\max}]},\xi^{[i^{\max}-1]},\dots,\xi^{[1]},\xi^{[0]}\right]} &= \left|\pm\xi^{[i^{\max}]} \cdot \mathcal{L}_{\mathrm{po}}^{[i^{\max}]} \pm \xi^{[i^{\max}-1]} \cdot \mathcal{L}_{\mathrm{po}}^{[i^{\max}-1]} \pm \cdots \pm \xi^{[1]} \cdot \mathcal{L}_{\mathrm{po}}^{[1]} \pm \xi^{[0]} \cdot \mathcal{L}_{\mathrm{po}}^{[0]}\right| \\ &= \left|\sum_{i=0}^{i^{\max}} \pm\xi^{[i]} \cdot \mathcal{L}_{\mathrm{po}}^{[i]}\right|.\end{aligned} \tag{7}$$

We call the set of binary variables $\Xi_{[k]} = \left[\xi^{[i^{\max}]}, \xi^{[i^{\max}-1]}, \dots, \xi^{[1]}, \xi^{[0]}\right]$ defining the pull-out height $\mathcal{H}_{\mathrm{po}}^{\Xi}$ its "*combination*" of pull-out lengths. The subscript k will be used whenever it is necessary to identify the number of hierarchical levels actually contributing to the pull-out height in a given combination (and omitted when otherwise), and it can be calculated as

$$k = \sum_{i=0}^{i^{\max}} \xi^{[i]}. \tag{8}$$

One extreme case for a combination is $\Xi_{[0]} = [0,0,\dots,0,0]$ and $k = 0$, which corresponds to a fibre with no contributions to its (zero) pull-out height; the other extreme case corresponds to a combination of $\Xi_{[i^{\max}+1]} = [1,1,\dots,1,1]$ and $k = i^{\max} + 1$, which represents a fibre with all individual hierarchical levels contributing to its pull-out height. In a fracture surface with maximum hierarchical level $i^{\max}$, there will be $i^{\max} + 1$ binary variables $\xi^{[i]}$ and, consequently, a total of $2^{i^{\max}+1}$ different combinations $\Xi_{[k]}$, with $0 \leq k \leq i^{\max} + 1$; for the particular case of $i^{\max} = 3$, the 16 different combinations are shown in Figure 4.

While the idealised fracture surface shown in Figure 4 features all pull-outs in the positive x-direction, Eq. 7 captures the (statistical) symmetry of real fracture surfaces, where pull-outs at

each individual level can occur in the positive or negative directions. This symmetry will not affect the energy dissipated in the formation of the fracture surfaces (since both debonding and friction areas are not affected by the direction of pull-out, as previously analysed) [5, 9]. However, to calculate pull-out height distributions, it is vital to consider that pull-out heights result from both the addition and subtraction of pull-out lengths of individual levels, as considering additions (or subtractions) only would overestimate pull-out heights (note that both $\mathcal{H}_{\mathrm{po}}$ and $\mathcal{L}_{\mathrm{po}}^{[i]}$ are defined as always positive, regardless of the direction of pull-out).

In addition to the relationship between pull-out heights and individual pull-out lengths defined in Eq. 7, to generate a statistical distribution of $\mathcal{H}_{\mathrm{po}}$ it is also necessary to identify the frequency of the different combinations Ξ. In total, for a fracture surface of level $i^{\max}$ with coordination number c, all combinations together must contribute with a total of $c^{i^{\max}+1}$ pull-out heights (since that is the number of fibres in the idealised fracture surface of that level, as illustrated in Figure 4). According to the Binomial Theorem, this number can be decomposed as follows:

$$\begin{aligned} c^{i^{\max}+1} &= [(c-1)+1]^{i^{\max}+1} \\ &= (c-1)^{i^{\max}+1} + (i^{\max}+1)\cdot(c-1)^{i^{\max}} + \mathcal{C}_{i^{\max}-1}^{i^{\max}+1}\cdot(c-1)^{i^{\max}-1} + \cdots \\ &\qquad + \mathcal{C}_{2}^{i^{\max}+1}\cdot(c-1)^{2} + (i^{\max}+1)\cdot(c-1) + 1 \\ &= \sum_{k=0}^{i^{\max}+1} \mathcal{C}_{k}^{i^{\max}+1}\cdot \nu_{[k]}, \text{ where } \nu_{[k]} = (c-1)^{i^{\max}+1-k}\,. \end{aligned} \tag{9}$$

In this equation, the coefficient $\mathcal{C}_{k}^{i^{\max}+1}$ is the binomial coefficient, or the number of distinct $k-$combinations (in the combinatorics sense, where k is the number of levels contributing to the pull-out height of a given fibre) from a set with $i^{\max}+1$ elements (i.e. the set of binary variables $\xi^{[i]}$). The factor $\nu_{[k]} = (c-1)^{i^{\max}+1-k}$ is the number of fibres which have a unique combination $\Xi_{[k]}$, i.e. the frequency of each individual $k-$combination.

Applying the definition of frequency $\nu_{[k]}$ in Eq. 9 to one extreme case, the combination $\Xi_{[i^{\max}+1]} = [1,1,\ldots,1,1]$ occurs $(c-1)^0 = 1$ time; this means that there is only one fibre on the fracture surface with all individual hierarchical levels contributing to its pull-out height. The other extreme case, with $\Xi_{[0]} = [0,0,\ldots,0,0]$, occurs $(c-1)^{i^{\max}+1}$ times; this means that there is a fraction of $[(c-1)/c]^{i^{\max}+1}$ fibres with zero pull-out height on the fracture surface. Table 2 defines the different combinations and their frequency for a generic fracture surface with maximum hierarchical level $i^{\max}$ and coordination number c; for the particular case of $i^{\max} = 3$ and $c = 9$, the frequencies of the different combinations are shown in Figure 4.

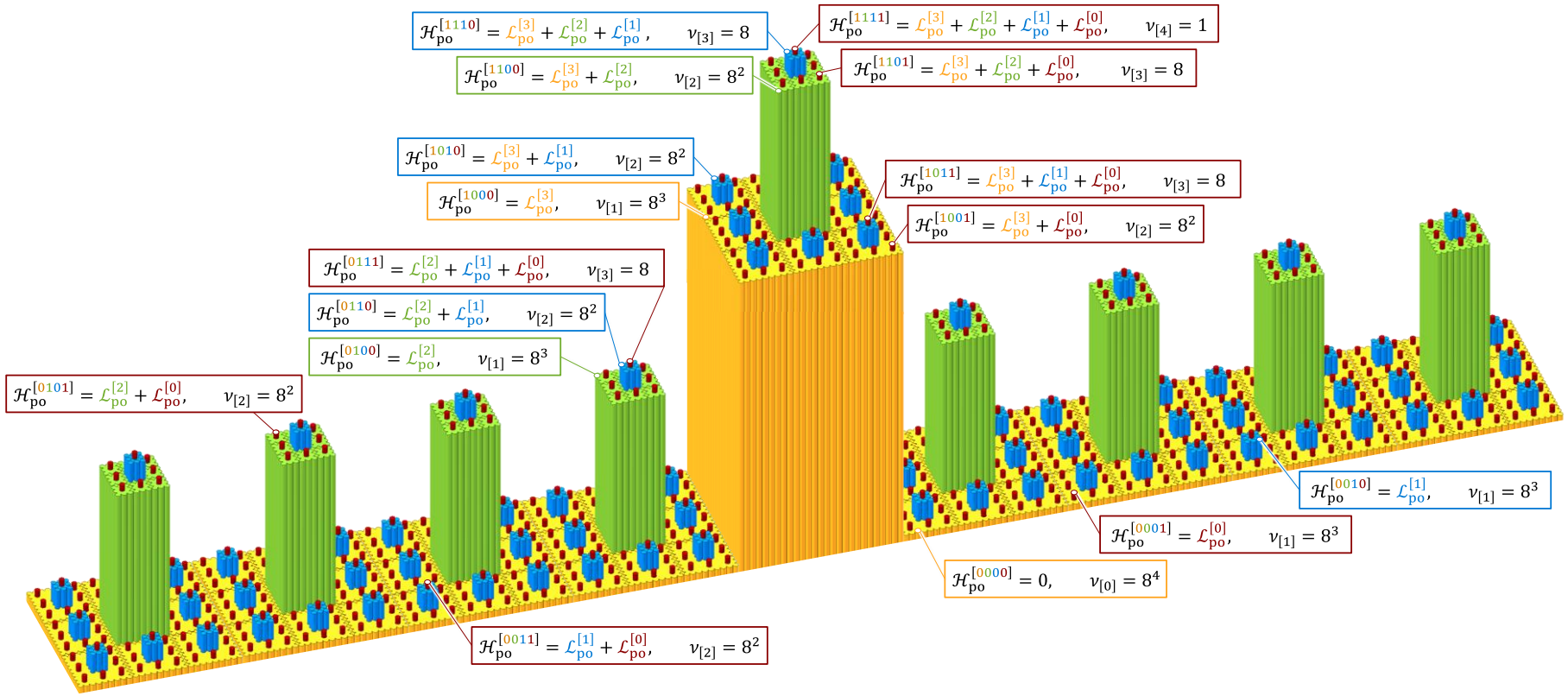

Figure 4: Idealised hierarchical fracture surface of a single 0° ply embedded in a laminate, with $c = 9$ and $i^{\max} = 3$, thus with a total of $c^{i^{\max}+1} = 9^4$ fibres. There are $2^{i^{\max}+1} = 16$ distinct expressions to calculate the pull-out height $\mathcal{H}_{\mathrm{po}}^{\Xi}$, and the same number of corresponding combinations $\Xi = \left[\xi^{[3]}, \xi^{[2]}, \xi^{[1]}, \xi^{[0]}\right]$. There is a single ($\mathcal{C}_0^4 = 1$) combination with no contributing individual levels (i.e. $k = 0$ and $\Xi_{[0]} = [0000]$), $\mathcal{C}_1^4 = 4$ distinct combinations with $k = 1$ contributing individual levels, $\mathcal{C}_2^4 = 6$ distinct combinations with $k = 2$ contributing individual levels, $\mathcal{C}_3^4 = 4$ distinct combinations with $k = 3$ contributing individual levels, and a single ($\mathcal{C}_4^4 = 1$) combination with all contributing individual levels (i.e. $k = 4$ and $\Xi_{[4]} = [1111]$). The frequency of each $k-$combination $\Xi_{[k]}$ is shown as $\nu_{[k]}$. Note that all fibres with $\xi^{[0]} = 0$ are surrounded by matrix fractured at the same height and thus represented by the same colour as the fibre itself.

Table 2: Definition of the relationship between pull-out lengths and pull-out heights, for an idealised fracture surface with generic maximum level $i^{\max}+1$ and coordination number c.

Number of levels contributing to the pull-out height, k	No. distinct combinations ($\mathcal{C}_k^{i^{\max}+1}$ represents the binomial coefficient)	Combination $\Xi_{[k]}$ of pull-out lengths $\xi^{[i^{\max}]}$	$\xi^{[i^{\max}-1]}$	…	$\xi^{[1]}$	$\xi^{[0]}$	Expression to calculate pull-out height from individual-level pull-out lengths	Frequency (no. fibres within total of $c^{i^{\max}+1}$)
$k=0$	$\mathcal{C}_0^{i^{\max}+1}=1$	0	0	…	0	0	$\mathcal{H}_{\mathrm{po}}^{[00\ldots00]}=0$	$(c-1)^{i^{\max}+1}$
$k=1$	$\mathcal{C}_1^{i^{\max}+1}=i^{\max}+1$	0	0	…	0	1	$\mathcal{H}_{\mathrm{po}}^{[00\ldots01]}=\mathcal{L}_{\mathrm{po}}^{[0]}$	$(c-1)^{i^{\max}}$
		0	0	…	1	0	$\mathcal{H}_{\mathrm{po}}^{[00\ldots10]}=\mathcal{L}_{\mathrm{po}}^{[1]}$	$(c-1)^{i^{\max}}$
		0	1	…	0	0	$\mathcal{H}_{\mathrm{po}}^{[01\ldots00]}=\mathcal{L}_{\mathrm{po}}^{[i^{\max}-1]}$	$(c-1)^{i^{\max}}$
		1	0	…	0	0	$\mathcal{H}_{\mathrm{po}}^{[10\ldots00]}=\mathcal{L}_{\mathrm{po}}^{[i^{\max}]}$	$(c-1)^{i^{\max}}$
$k=2$	$\mathcal{C}_2^{i^{\max}+1}$	0	0	…	1	1	$\mathcal{H}_{\mathrm{po}}^{[00\ldots11]}=\left\lvert \mathcal{L}_{\mathrm{po}}^{[1]} \pm \mathcal{L}_{\mathrm{po}}^{[0]} \right\rvert$	$(c-1)^{i^{\max}-1}$
		0	1	…	0	1	$\mathcal{H}_{\mathrm{po}}^{[01\ldots01]}=\left\lvert \mathcal{L}_{\mathrm{po}}^{[i^{\max}-1]} \pm \mathcal{L}_{\mathrm{po}}^{[0]} \right\rvert$	$(c-1)^{i^{\max}-1}$
		1	0	…	0	1	$\mathcal{H}_{\mathrm{po}}^{[10\ldots01]}=\left\lvert \mathcal{L}_{\mathrm{po}}^{[i^{\max}]} \pm \mathcal{L}_{\mathrm{po}}^{[0]} \right\rvert$	$(c-1)^{i^{\max}-1}$
		0	1	…	1	0	$\mathcal{H}_{\mathrm{po}}^{[01\ldots10]}=\left\lvert \mathcal{L}_{\mathrm{po}}^{[i^{\max}-1]} \pm \mathcal{L}_{\mathrm{po}}^{[1]} \right\rvert$	$(c-1)^{i^{\max}-1}$
		1	0	…	1	0	$\mathcal{H}_{\mathrm{po}}^{[10\ldots10]}=\left\lvert \mathcal{L}_{\mathrm{po}}^{[i^{\max}]} \pm \mathcal{L}_{\mathrm{po}}^{[1]} \right\rvert$	$(c-1)^{i^{\max}-1}$
		1	1	…	0	0	$\mathcal{H}_{\mathrm{po}}^{[11\ldots00]}=\left\lvert \mathcal{L}_{\mathrm{po}}^{[i^{\max}]} \pm \mathcal{L}_{\mathrm{po}}^{[i^{\max}-1]} \right\rvert$	$(c-1)^{i^{\max}-1}$
k	$\mathcal{C}_k^{i^{\max}+1}$							$(c-1)^{i^{\max}+1-k}$
$k=i^{\max}$	$\mathcal{C}_{i^{\max}}^{i^{\max}+1}=i^{\max}+1$	1	1	…	1	0	$\mathcal{H}_{\mathrm{po}}^{[11\ldots01]}=\left\lvert \mathcal{L}_{\mathrm{po}}^{[i^{\max}]} \pm \mathcal{L}_{\mathrm{po}}^{[i^{\max}-1]} \pm \cdots \pm \mathcal{L}_{\mathrm{po}}^{[1]} \pm 0 \right\rvert$	$(c-1)^1$
		1	1	…	0	1	$\mathcal{H}_{\mathrm{po}}^{[11\ldots01]}=\left\lvert \mathcal{L}_{\mathrm{po}}^{[i^{\max}]} \pm \mathcal{L}_{\mathrm{po}}^{[i^{\max}-1]} \pm \cdots \pm 0 \pm \mathcal{L}_{\mathrm{po}}^{[0]} \right\rvert$	$(c-1)^1$
		1	0	…	1	1	$\mathcal{H}_{\mathrm{po}}^{[10\ldots11]}=\left\lvert \mathcal{L}_{\mathrm{po}}^{[i^{\max}]} \pm 0 \pm \cdots \pm \mathcal{L}_{\mathrm{po}}^{[1]} \pm \mathcal{L}_{\mathrm{po}}^{[0]} \right\rvert$	$(c-1)^1$
		0	1	…	1	1	$\mathcal{H}_{\mathrm{po}}^{[01\ldots11]}=\left\lvert 0 \pm \mathcal{L}_{\mathrm{po}}^{[i^{\max}-1]} \pm \cdots \pm \mathcal{L}_{\mathrm{po}}^{[1]} \pm \mathcal{L}_{\mathrm{po}}^{[0]} \right\rvert$	$(c-1)^1$
$k=i^{\max}+1$	$\mathcal{C}_{i^{\max}+1}^{i^{\max}+1}=1$	1	1	…	1	1	$\mathcal{H}_{\mathrm{po}}^{[11\ldots11]}=\left\lvert \mathcal{L}_{\mathrm{po}}^{[i^{\max}]} \pm \mathcal{L}_{\mathrm{po}}^{[i^{\max}-1]} \pm \cdots \pm \mathcal{L}_{\mathrm{po}}^{[1]} \pm \mathcal{L}_{\mathrm{po}}^{[0]} \right\rvert$	$(c-1)^0=1$

4.2.3 Stochastic distributions of pull-out lengths

The second challenge identified in Section 4.2.1 will be addressed by performing an inverse transform sampling method on the cumulative distribution functions of pull-out lengths $\mathcal{F}_{\mathrm{po}}^{[i]}\left(l_{\mathrm{po}}^{[i]}\right)$ predicted by Pimenta and Pinho's original toughness model [9]. This method requires the following steps:

(i) Implementing Pimenta and Pinho's model to compute the numerical cumulative distribution function for pull-out length $\mathcal{F}_{\mathrm{po}}^{[i]}\left(l_{\mathrm{po}}^{[i]}\right)$ for each level-$[i]$ (see Figure 5 (a)).

(ii) For each hierarchical level $0 \leq i \leq i^{\max}$, calculate a set of $\eta^{[i]}$ uniformly distributed random variables in the interval [0,1], i.e. $\mathcal{U}\sim$Unif[0,1], where $\eta^{[i]}$ is the number of stochastic pull-out lengths to be sampled according to $\mathcal{F}_{\mathrm{po}}^{[i]}\left(l_{\mathrm{po}}^{[i]}\right)$ (which will be defined in the next paragraph).

(iii) Use the numerical definition of $\mathcal{F}_{\mathrm{po}}^{[i]}\left(l_{\mathrm{po}}^{[i]}\right)$ calculated in (i) to map from the $\eta^{[i]}$ uniform random variables $\mathcal{U}$ to $\eta^{[i]}$ stochastic pull-out lengths $\mathcal{L}_{\mathrm{po}}^{[i]}$, as $\mathcal{L}_{\mathrm{po}}^{[i]} = {\mathcal{F}_{\mathrm{po}}^{[i]}}^{-1}(\mathcal{U})$ (as illustrated in Figure 5(b)).

To generate an entire fracture surface of maximum level $i^{\max}+1$, the number of times that the pull-out length distribution of an individual level i needs to be sampled for random pull-out lengths ($\eta^{[i]}$) is the sum of the frequencies of all combinations including the contribution of that level, i.e. with $\xi^{[i]} = 1$. According to the following considerations,

- the frequency of each combination $\Xi_{[k]}$ is equal to $\nu_{[k]} = (c-1)^{i^{\max}+1-k}$, as defined in Eq. 9,
- these frequencies must be summed for all combinations with $1 \leq k \leq i^{\max}+1$, (i.e. excluding $k = 0$, since there is no need to sample pull-out lengths for the all-zeros combination, which has a zero pull-out height $\mathcal{H}_{\mathrm{po}}^{[0,0,\ldots,0,0]} = 0$),
- the number of $k-$combinations containing $\xi^{[i]} = 1$ is $\mathcal{C}_{k-1}^{i^{\max}}$, corresponding to the selection of the remaining $k-1$ contributing levels (in addition to level i) from the set of $i^{\max}$ available levels,

then $\eta^{[i]}$ is independent of i, and can be defined as

$$\begin{aligned}\eta &= \sum_{k=1}^{i^{\max}+1} \mathcal{C}_{k-1}^{i^{\max}} \cdot (c-1)^{i^{\max}+1-k} \text{ and, replacing } k' = k-1,\\ &= \sum_{k'=0}^{i^{\max}} \mathcal{C}_{k'}^{i^{\max}} \cdot (c-1)^{i^{\max}-k'} \text{ which, according to the Binomial Theorem,}\\ &= c^{i^{\max}}.\end{aligned} \tag{10}$$

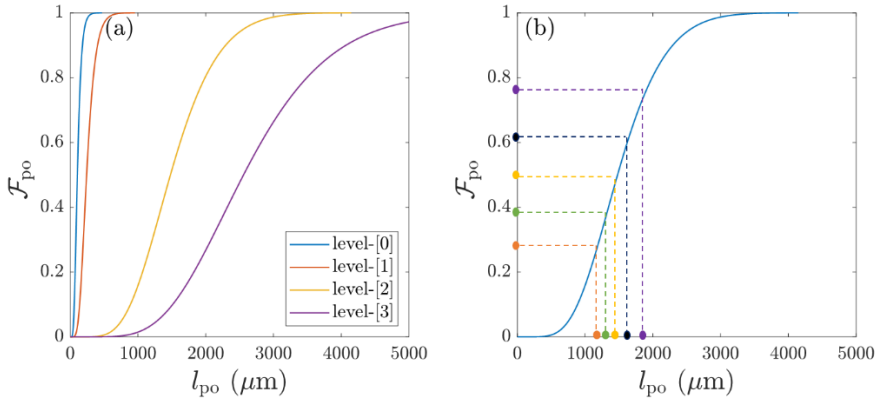

Figure 5: Generation of stochastic distributions of pull-out lengths as explained in Section 4.2.3.
(a, left) Cumulative distribution functions of pull-out length for distinct hierarchical levels, calculated as explained in Point (i).
(b, right) Inverse transform sampling method for a single hierarchical level as explained in Points (ii)-(iii).

4.2.4 Calculation of pull-out height distributions and model implementation

Sections 4.2.2 and 4.2.3 describe the methodology to generate a set of $c^{i^{\max}+1}$ stochastic values of pull-out heights $\mathcal{H}_{\mathrm{po}}$; this set corresponds to the statistical cumulative distribution function predicted by the model, which can be represented as

$$\mathbb{H}\left(h_{\mathrm{po}}\right) = \Pr\left(\mathcal{H}_{\mathrm{po}} \leq h_{\mathrm{po}}\right). \tag{11}$$

This methodology can be implemented efficiently with the algorithm shown in Figure 6, thus addressing the third challenge identified in Section 4.2.1.

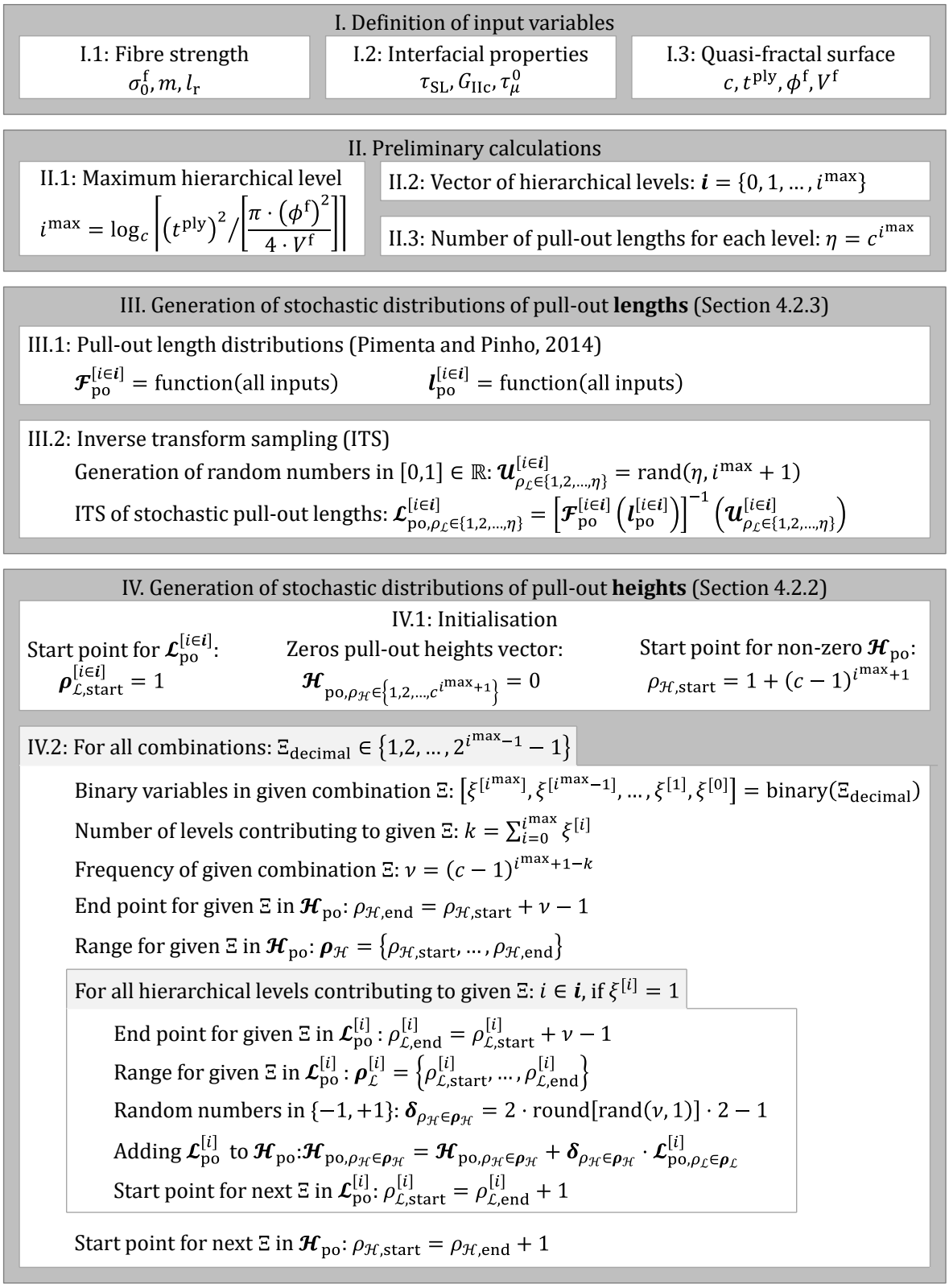

Figure 6: Flowchart with the algorithm implementation of the model to predict pull-out distributions described in Section 4.

4.3 Predicting temperature's effect on the translaminar fracture toughness and pull-out height distributions

Pimenta and Pinho's model assumes that stresses are constantly redistributed on the fibres and bundles bridging the crack front during the translaminar failure process, as the failure evolves down the hierarchical levels (i.e. from level-$[i+1]$ to level-$[i]$ and then level-$[i-1]$). Stress analyses [9] have shown that the interfacial properties (including shear strength τ_{SL}, mode-II toughness G_{IIc}, and frictional stress τ_{μ}) are key parameters in determining how stresses redistribute around broken fibres and bundles, which consequently influence the model prediction of the energy dissipated through debonding and pull-out. Given that these interfacial properties are substantially affected by variations in temperature [5], using temperature-dependent values of τ_{Sl}, G_{IIc}, and τ_{μ} as model inputs will generate temperature-dependent values of the translaminar fracture toughness and pull-out length distributions, as model outputs.

The relationship between interfacial properties and temperature has been derived in our previous study [5] on a similar type of aerospace CFRP composite, through a combination of experiments and micromechanical models. We assume that the same proportional effect previously verified for interfacial properties as a function of temperature also applies to the current material studied in this present paper. Table 1 has listed the corresponding values of τ_{Sl}, G_{IIc}, and τ_{μ} for the three testing temperatures considered here, which are used as inputs to account for the temperature's effect on the translaminar fracture toughness and pull-out height distributions.

5 Results

5.1 Effect of temperature on translaminar fracture toughness

Representative load-displacement curves from the compact tension tests at three different temperatures (Figure 7) clearly show increasing nonlinearity with rising temperature.

The translaminar fracture toughness of the laminate measured at different temperatures is shown in Figure 8, which indicates a strong *R*-curve effect for all conditions. The propagation translaminar toughness was estimated by averaging the peak points of each short segment in the plateaued region of the *R*-curves for the -55°C and 23°C tests. At 90°C, the *R*-curves exhibited a continuous rising trend up to a crack growth of approximately 4 mm, after which there were no valid data points due to compressive failure at the unnotched region; therefore, the maximum observed value for toughness (represented as a propagation line in Figure 8 (c)) indicates a lower bound for the propagation translaminar toughness at 90°C.

The 0°-ply-level translaminar fracture toughness for crack propagation was calculated based on the rule of mixtures in Eq. 4 and is presented in Table 3. The results show that elevated temperature leads to an increase in translaminar fracture toughness. The translaminar fracture toughness exhibited an almost threefold increase with temperature from -55°C to 90°C.

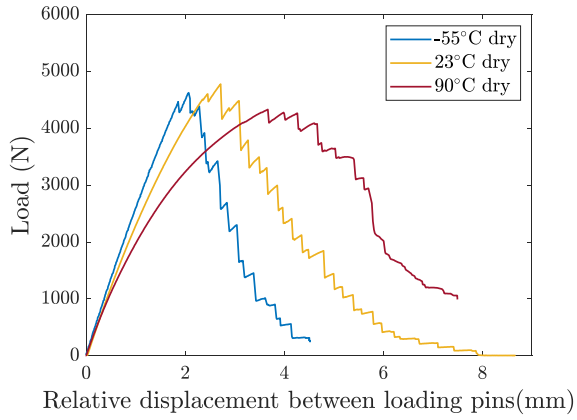

Figure 7: Representative load-displacement curves for compact-tension testing under each temperature.

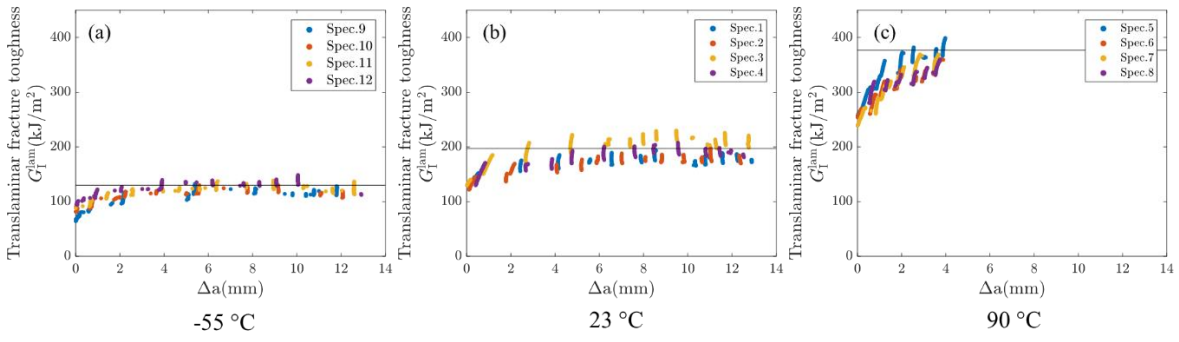

Figure 8: *R*-curves obtained under each temperature. The horizontal line indicates the estimated average propagation toughness.

Table 3. Summary of 0°-ply-level translaminar toughness, G_{Ic}^{0}, at different temperatures (the value for 90°C represents a lower bound of the apparent experimental value associated with this compact tension specimen geometry).

Temperature	-55°C	23°C	90°C
0°-ply-level translaminar toughness (kJ/m^2)	271 ± 18	411 ± 35	788

Figure 9 shows the comparison between the experimentally determined translaminar fracture toughness and the corresponding model predictions for each temperature. While the model prediction is in good agreement with the experimental results at 23°C, it slightly overestimates and considerably underestimates the translaminar fracture toughness at -55°C and 90°C respectively. These differences will be discussed in Section 6.3.

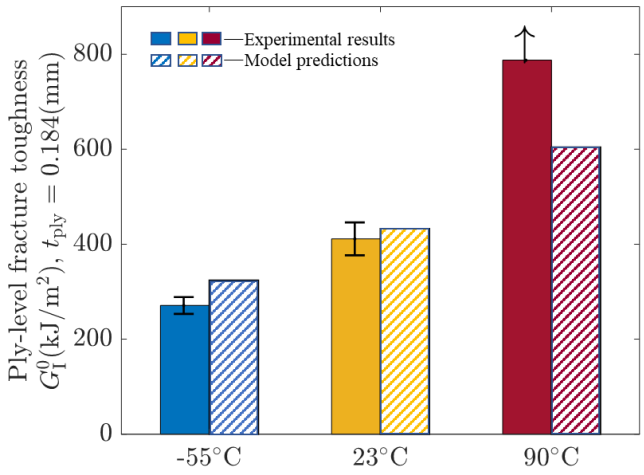

Figure 9: Comparison between model predictions and experimental results of G_I^0 for each temperature.

5.2 3D visualization of fracture surfaces and quantification of pull-out heights

Figure 10 shows the pull-out height mapped on the fracture surfaces created under three different temperatures, following the computed-tomography scanning and post-processing methodology detailed in Section 3.2. The fracture surfaces clearly show that, under elevated temperature, fibre pull-out becomes significantly more extensive.

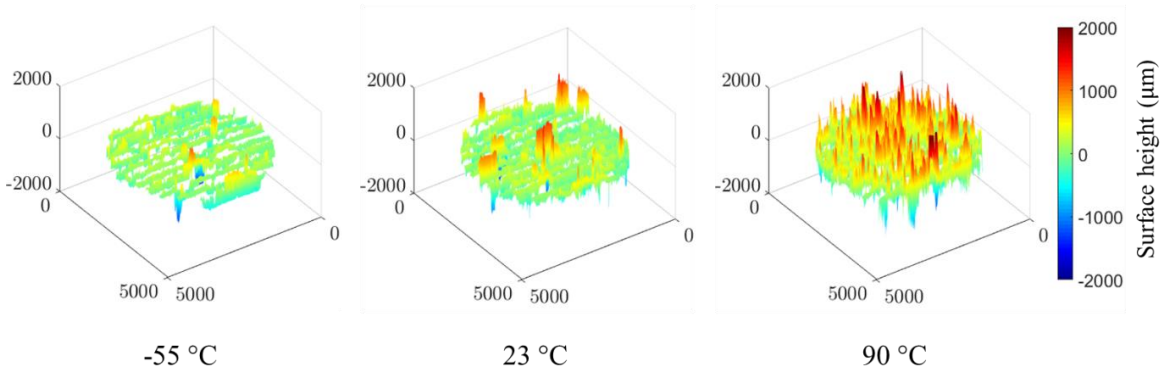

Figure 10: 3D visualization of pulled-out fibres and bundles developed on 0° plies for each temperature. (All dimensions in µm)

5.3 Comparison of model predicted and experimentally measured pull-out height distributions

The absolute values of the surface heights in Figure 10 were translated into the cumulative probability curves in Figure 11, where experimental and predicted results are compared for all three temperatures. The experimentally measured pull-out heights were distributed within a range of pull-out heights up to 1.2 mm for -55°C, 1.6 mm for 23°C, and 2.5 mm for 90°C. In comparison, the model predicts that 89.0% of pull-out heights are below 1.2 mm for -55°C, 85.3% below 1.6 mm for 23 °C, and 85.2% below 2.5mm for 90 °C respectively, therefore

resulting in an overall accuracy of more than 85%. The model captures the trend of increasing pull-out heights with increasing temperature, and it also predicts pull-out heights in the same order of magnitude as observed in the experiments; however, the distributions predicted by the model have a tail with larger pull-out heights than those observed in the experiments, and also a different shape (these differences will be discussed in Section 6.2).

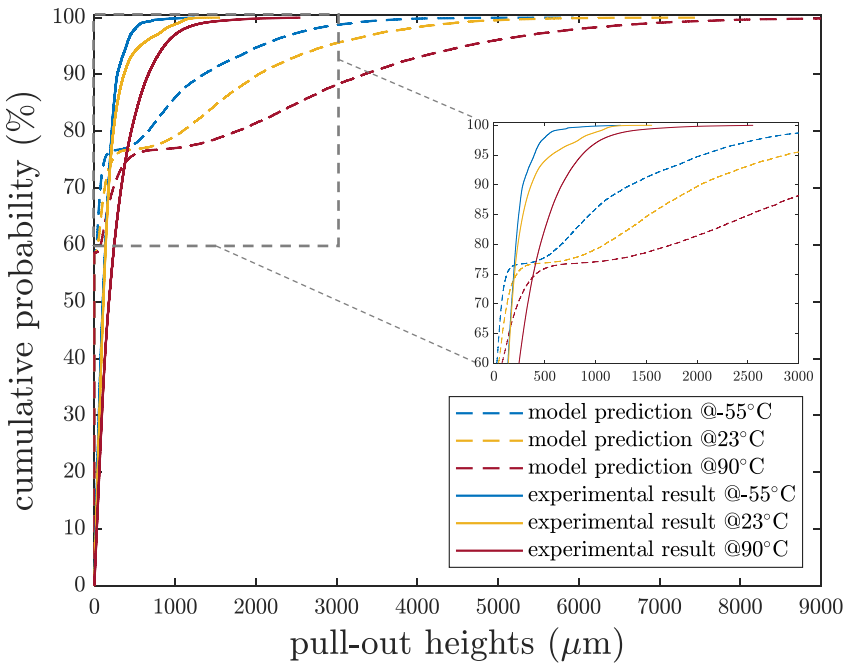

Figure 11: Comparison between model prediction and experimental measurements of cumulative probability for pull-out lengths at each temperature.

Considering that the experimentally-measured pull-out heights range between 0 and 3 mm in Figure 11, it would be interesting to show the relative probability of pull-out heights in that range. To this end, histograms in Figure 12 are plotted by grouping experimental/predicted data into bins of equal width (10 μm); each bin is plotted as a bar with its height corresponding to the percentage of data that falls in that range, thus indicating the frequency of certain pull-out heights. The experimental histograms are characterised by a peak located around relatively shorter pull-out heights followed by a tail that expands to longer pull-out heights; the height of the peak reduces while the length of the tail increases as the temperature increases. A similar trend can be observed in the model predictions, although some differences can be noted:

- The predicted histograms have a vertical spike at $h_{\mathrm{po}} = 0$; this corresponds to the large percentage of zero pull-out height predicted by the model (corresponding to the combination $\Xi_{[0]} = [0,0,0,0]$), which is also shown in the cumulative probability curves in Figure 11;
- The predicted histograms have two peaks: a more prominent one at small pull-out heights (below 100 μm for all temperatures), and a less prominent one at larger pull-out heights (between 0.8 and 2.6 mm).

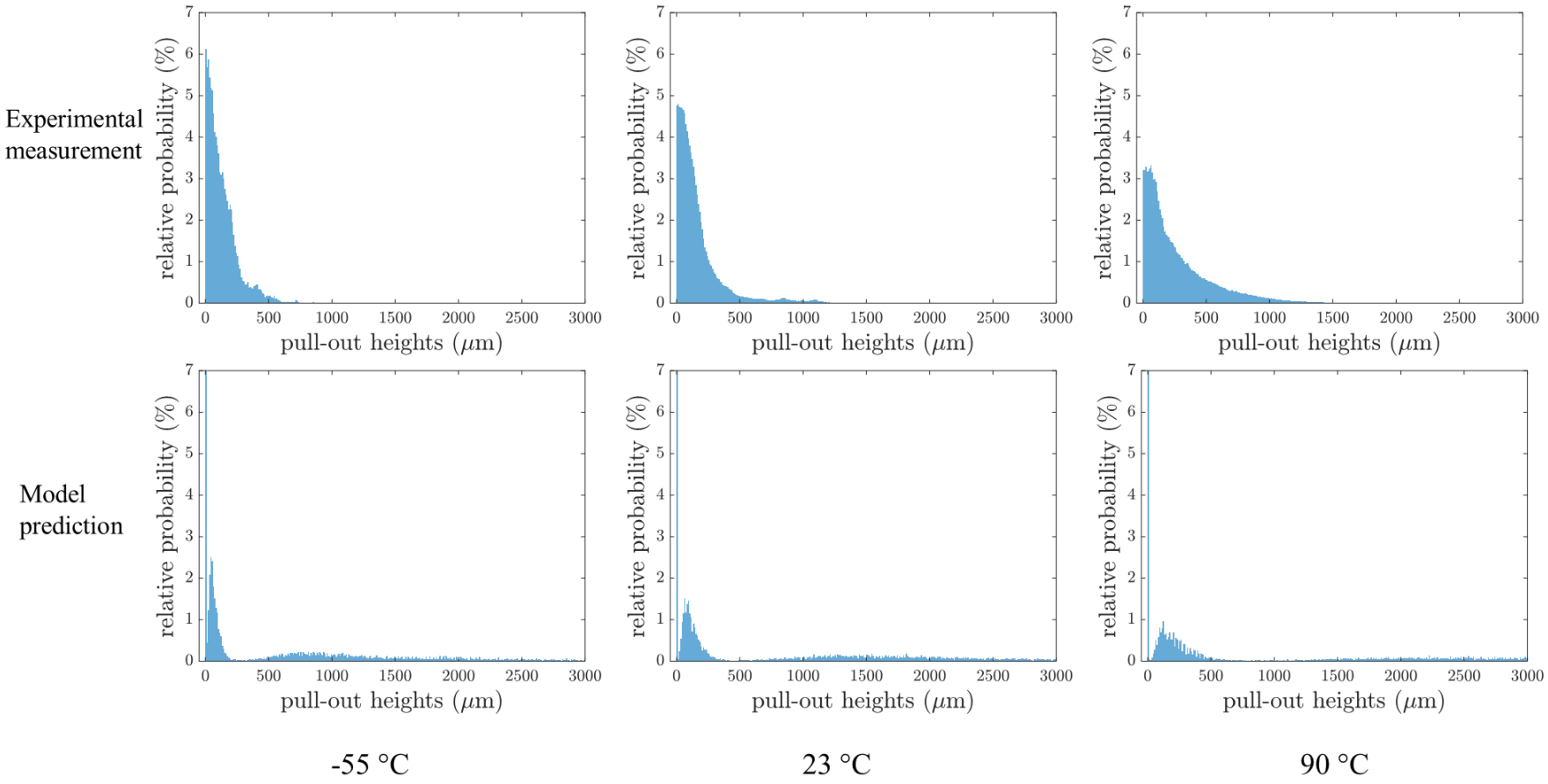

Figure 12: Histograms of pull-out height distributions, which show the frequency of each pull-out height in the experimental measurements and model predictions for the three temperatures.

5.4 Effect of interfacial properties on the prediction of pull-out length distribution

The model inputs associated with temperature-dependent interfacial properties (i.e. mode-II interlaminar toughness G_{IIc}, pull-out frictional stress τ_μ, and interfacial shear strength τ_{SL}) are difficult to estimate, but they have a significant impact on the predictions not only for the propagation toughness [5], but also for pull-out height distributions. Therefore, Figure 13 is a sensitivity study showing the effect of the three interfacial properties on the predicted pull-out height distribution for specimens tested under 23°C. Figure 13 (a) shows that, with an increasing G_{IIc}, both the first peak and the second peak become increasingly prominent, and closer to each other, with a smaller upper tail. As shown in Figure 13 (b), while τ_μ has a relatively minor effect on the first peak, it strongly influences the second peak, which becomes more prominent and moves towards shorter pull-outs with increasing τ_μ. The opposite effect can be seen in Figure 13 (c), where the second peak moves into larger pull-out heights as τ_{SL} increases.

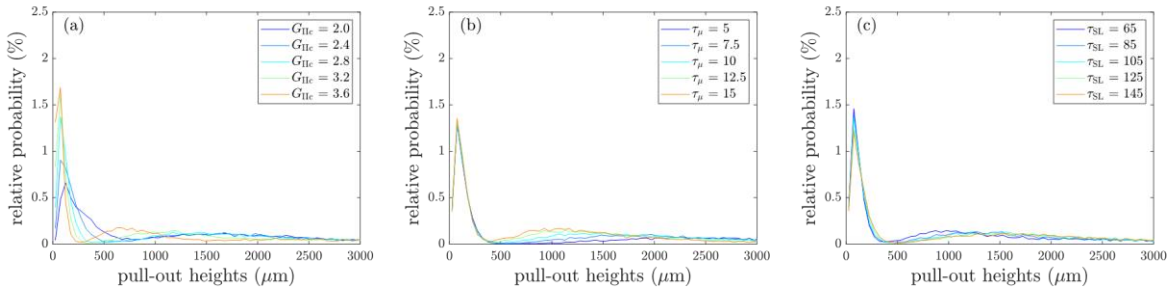

Figure 13: Effect of interfacial properties on the predicted pull-out length distribution. The nominal interfacial properties used in this study correspond to the inputs for the 23°C case.

6 Discussion

6.1 Methodology proposed to measure pull-out heights and experimental results

This study has proposed a comprehensive approach to imaging and quantifying the fracture surfaces of compact tension specimens using high-resolution 3D images obtained by xCT. Such a quantitative analysis of fibre pull-out is implemented for the first time and gives more insights than the 2D analyses previously carried out in the literature [1, 4, 8, 9] in several aspects:

(i) The pull-outs of fibres/bundles are stochastic, multiscale and hierarchical in nature. While local inspection of small regions by 2D imaging could potentially introduce statistical and scale biases, the global and 3D nature of xCT imaging, together with the objective data-processing methodology proposed in Section 3.2, address this difficulty by extracting the full 3D morphological information of a representative fracture surface.

(ii) The quantitative analysis of xCT images provides an accurate map of the varying pull-out heights across the scanned fracture surface and reveals the effect of temperature on the pull-out height distributions.

(iii) This approach could be applied to other studies: for instance, it would be useful to do a comparative study on the pull-out height distributions in FRPs with different fibres, matrices, or interfaces. This would provide quantitative knowledge of the

pull-out toughening mechanism, which is fundamental to the design of tougher composites.

The distributions of pull-out heights in Figure 11 show much longer pull-outs than those predicted in the literature [7], which is probably because most of the models [8, 16, 17] were proposed by considering the pull-out of individual fibres only, which tend to occur with short lengths. However, it is clearly shown in Figure 2 that bundles with various sizes are pulled-out. This highlights the importance of considering the entire range of pulled-out bundles in the present model, as their heights can potentially cover multiple length scales.

It is worth mentioning that, due to the lack of image contrast and morphological features, pixels at the 0° and 90° plies interfaces are easily mislabelled as belonging to the wrong ply, as shown in Figure 2(e). This clearly exemplifies why simple segmentation algorithms cannot accurately define the boundaries between 0° and 90° plies. Although it is inevitable to introduce errors, the method proposed in Section 3.2 gives the best possible estimates of the distribution of pull-out heights and offers a consistent way of data processing without manual (and, therefore, potentially biased) interventions. As the field of characterising the micro- and meso-structure of FRPs with xCT progresses further, this method can be benchmarked against others, in terms of computational efficiency and accuracy.

As mentioned in Section 3.1, in total there are more than 150,000 individual fibres in the scanned volume, which is equivalent to more than 300 level-[3] bundles (the largest bundle size considered in the model as indicated by Equation 6 and Figure 4). Therefore, such large number of fibres in the scanned volume provides statistical significance to the present experimental observations.

6.2 Methodology proposed to predict pull-out heights

The present study has proposed a model to predict pull-out height distributions based on the analysis of quasi-fractal fracture surfaces. It is the first model that considers not only the stochastic pull-out length of individual fibres but also that of bundles with various sizes. The comparisons between the experimental data and model predictions indicate several important implications:

(i) As shown in Figure 11, the cumulative probability curves for the experimentally measured pull-out heights increase smoothly for all three temperatures. By contrast, the model overpredicts both tails of the cumulative probability curves: it predicts a vertical increase at zero pull-out height up to nearly 60% probability (corresponding to the combination $\Xi_{[0]} = [0,0,0,0]$ and a fraction of $[(c-1)/c]^{i^{\max}+1}$ as explained in Section 4.2.2), whereas the rest of the curves follow a distribution with two peaks over a wider range of pull-out heights. This can be attributed to the model's assumption of discrete hierarchical levels of pull-out across the range of scales in the fracture surface (see Figure 4), where only one out of c fibres or bundles pull out from their neighbours; on the contrary, the experimental fracture surfaces feature pull-outs distributed continuously over the range of scales. Nevertheless, the effects of temperature observed experimentally – namely the increase in both average and variability of pull-out heights – is captured correctly by the model.

(ii) The experimental cumulative probability curves in Figure 11 show that an increase in temperature has caused a larger average and larger variability for experimentally measured pull-out heights; this temperature dependence has been successfully predicted by the model, which suggests that the model captures the main

mechanisms governing the failure and pull-out processes. This effect of temperature on pull-out height distributions may be explained by the fact that interfacial properties vary with temperature – the shear strength τ_{SL}, the mode-II toughness G_{IIc}, and the frictional stress τ_{μ} all decrease with increasing temperature [9] – which consequently affects the stress field during the debonding and pull-out process.

(iii) The effect of each interfacial property on pull-out height distributions is further detailed in Figure 13.

a. Pull-out heights are necessarily bound by debonding heights, which are largely dependent on G_{IIc}. As G_{IIc} increases, debonding is arrested, which subsequently restricts the development of pull-out, as shown in Figure 13(a).

b. Once debonding has occurred, stress concentrations in bridging bundles (which will eventually form pull-outs) develop through friction. A large τ_{μ} would impose a large stress gradient, and thus a small stress concentration length in the bridging bundle, within the debonded region [9]. Therefore, the debonded bridging bundles, which are likely to break in the region of stress concentrations, would fail with minimal pull-out lengths, if τ_{μ} is large. Evidence for this can be seen in Figure 13(b), where the second peak of pull-out heights moves to smaller values as τ_{μ} increases, while the first peak remains unaffected; this difference indicates that failure of the bridging fibres and bundles happens before debonding for small hierarchical levels (when stress gradients are affected by τ_{SL} rather than by τ_{μ}), but after debonding for large hierarchical levels.

c. The increase in pull-out heights with increasing τ_{SL} shown in Figure 13(c) is opposite to what would be expected just from a shear-lag analysis: a larger τ_{SL} would decrease the stress concentration length in bridging fibres and bundles before debonding, which should promote smaller pull-out heights. Instead, the governing effect is that an increase in τ_{SL} leads to an increase in the average strength distributions of fibres and bundles [23], which promotes failure of bridging fibres and bundles at higher loads (when extensive debonds can be formed), consequently leading to longer pull-outs.

These effects highlight the complex role of the fibre/matrix interface in controlling the pull-out height distribution.

6.3 Model validation for translaminar fracture toughness

As seen in Figure 9, the increasing trend of translaminar fracture toughness with temperature has been successfully captured by the model. A good agreement was found between the predicted and experimentally measured translaminar fracture toughness for 23°C, whereas there was a significant mismatch for 90°C (and, to a smaller extent, for -55°C). These differences may be explained by several reasons:

(i) There is a scarcity of available interfacial property data (including τ_{SL} and G_{IIc}) for the studied material, especially at -55°C and 90°C, in the literature, which inevitably constrains the accuracy of the model predictions. The influence of interfacial properties has been quantified and discussed through a sensitivity analysis presented in our previous work [5].

(ii) As discussed in [5], cross-ply compact tension specimens tested under high temperatures (e.g. 90°C) are susceptible to large-scale energy-dissipation mechanisms, such as shear non-linearity at the loading arms, and premature failure under compression at the back of the specimen. Consequently, the apparent fracture

toughness measured under those conditions is an overestimation of the actual translaminar fracture toughness of the composite (because it includes the energy dissipated by the shear non-linearity at the arms, which does not contribute to the translaminar fracture process). Conversely, the lack of a stable plateau in the R-curves shown in Figure 8c indicates that the maximum energy release rate reached in the tests at 90°C is a lower bound of the apparent toughness (as indicated in the caption of Table 3). While it is impossible to know which of these two opposite effects is dominant, the very strong non-linearity shown in the load-displacement curve for the 90°C specimen suggests that the value of fracture toughness indicated in Table 3 and Figure 9 for 90°C testing is actually an overestimation of the real translaminar toughness of the material.

(iii) The present model considers debonding and pull-out as the main toughening mechanisms, while neglecting the presence of other energy-dissipation mechanisms associated with translaminar fracture (such as non-linear deformation of the matrix, fibre fracture, and stress redistribution near the crack tip). Nevertheless, the role of these other energy-dissipation mechanisms could become more significant with increasing temperature, giving rise to extra energy dissipation and therefore increasing the translaminar toughness. These unaccounted mechanisms could be additional reasons why the model underestimates the translaminar fracture toughness at 90°C.

6.4 Relationship between the extent of fibre pull-out and translaminar fracture toughness

The 3D fracture surfaces visualised in Figure 10, together with the fibre pull-out height distributions shown in Figure 11 and Figure 12, show that higher testing temperature led to a more extensive development of fibre pull-out, with more fibres protruded from the global crack plane and larger pull-out heights. The larger heights are consistent with the increasing trend of translaminar fracture toughness, and the mechanism can be explained as follows: (i) the exposure of composites to elevated temperatures can severely undermine the fibre/matrix interface (as evidenced by SEM images of the fibre/matrix interface [4, 26, 27]); (ii) weaker interfaces in turn provide less resistance to the interfacial debonding and subsequent pull-out process; (iii) therefore, longer pull-out lengths develop on the fracture surfaces formed under higher temperatures, which ultimately leads to a higher energy dissipation.

It is interesting to note that, although the interfacial properties that govern energy dissipation (G_{IIc} and τ_{μ}) decrease with increasing temperature, they actually generate an increase in the translaminar fracture toughness of composites, due to the increase in pull-out (and debonding) heights.

7 Conclusion

The presented work provides a comprehensive study to understand the relationship between translaminar fracture toughness and pull-out height distribution based on the following experimental and modelling methodologies:

- xCT was performed to obtain a detailed 3D image of the fracture surface, which accurately maps the stochastic pull-out heights over the scanned surface. An image processing method is proposed to quantify the pull-out height distributions using the tomography images. Such analysis is performed here for the first time and can

be exploited for future studies on the toughening mechanisms of different material systems.

- This study presents the first analytical approach to predict the distribution of pull-out heights accounting for the wide range of scales observed in fracture surfaces. By using the analogy of quasi-fractal fracture surfaces and applying the inverse transform sampling method, the stochastic pull-out lengths were generated for each hierarchical level, which were later combined in a computationally-efficient algorithm to compute the pull-out heights of individual fibres and bundles with various sizes.

In order to validate model predictions against experimental measurements, cross-ply compact-tension experiments were carried out under three temperatures: −55 °C, 23 °C, and 90 °C, which were followed by quantitative analysis of pull-out height distributions. The following concluding remarks can be drawn:

- The model has successfully captured the trend of increasing pull-out lengths with increasing temperature (and, consequently, of translaminar fracture toughness) observed in the experiments.
- The increase in the translaminar fracture toughness observed with increasing temperatures is strongly related to the more extensive fibre pull-out.
- Compared to the cumulative probability of pull-out heights obtained from experiments, the model predictions resulted in accuracies of 89.0%, 85.3% and 85.2% at −55 °C, 23 °C, and 90 °C respectively.

Acknowledgements

Funding from Innovate UK, ATI and Rolls-Royce plc via the collaborative research projects "CTI Composite Fan Technology" (113085) and "FANTASTICAL" (113190) is gratefully acknowledged. The X-ray computed tomography experiments were supported by the National Research Facility for lab X-ray Computed Tomography (NXCT) through EPSRC grant EP/T02593X/1.

References

1. Pinho, S.T., P. Robinson, and L. Iannucci, *Fracture toughness of the tensile and compressive fibre failure modes in laminated composites.* Composites science and technology, 2006. **66**(13): p. 2069-2079.
2. Laffan, M., et al., *Measurement of the in situ ply fracture toughness associated with mode I fibre tensile failure in FRP. Part I: Data reduction.* Composites science and technology, 2010. **70**(4): p. 606-613.
3. Laffan, M., et al., *Measurement of the in situ ply fracture toughness associated with mode I fibre tensile failure in FRP. Part II: Size and lay-up effects.* Composites Science and Technology, 2010. **70**(4): p. 614-621.
4. Marín, L., et al., *Hygrothermal effects on the translaminar fracture toughness of cross-ply carbon/epoxy laminates: failure mechanisms.* Composites Science and Technology, 2016. **122**: p. 130-139.
5. Yu, B., et al., *Hygrothermal effects on the translaminar fracture toughness of a highly toughened aerospace CFRP: Experimental characterisation and model prediction.* Composites Part A: Applied Science and Manufacturing, 2021. **150**: p. 106582.
6. Teixeira, R., S. Pinho, and P. Robinson, *Thickness-dependence of the translaminar fracture toughness: experimental study using thin-ply composites.* Composites Part A: Applied Science and Manufacturing, 2016. **90**: p. 33-44.
7. Kim, J.-K. and Y.-W. Mai, *High strength, high fracture toughness fibre composites with interface control—a review.* Composites Science and Technology, 1991. **41**(4): p. 333-378.
8. Wells, J. and P. Beaumont, *Debonding and pull-out processes in fibrous composites.* Journal of Materials Science, 1985. **20**(4): p. 1275-1284.
9. Pimenta, S. and S.T. Pinho, *An analytical model for the translaminar fracture toughness of fibre composites with stochastic quasi-fractal fracture surfaces.* Journal of the Mechanics and Physics of Solids, 2014. **66**: p. 78-102.
10. Withers, P.J. and M. Preuss, *Fatigue and damage in structural materials studied by X-ray tomography.* annual review of materials research, 2012. **42**: p. 81-103.
11. Maire, E. and P.J. Withers, *Quantitative X-ray tomography.* International materials reviews, 2014. **59**(1): p. 1-43.
12. Garcea, S., et al., *Mapping fibre failure in situ in carbon fibre reinforced polymers by fast synchrotron X-ray computed tomography.* Composites Science and Technology, 2017. **149**: p. 81-89.
13. Bull, D., et al., *A comparison of multi-scale 3D X-ray tomographic inspection techniques for assessing carbon fibre composite impact damage.* Composites Science and Technology, 2013. **75**: p. 55-61.
14. Rinaldi, R.G., et al., *Generating virtual textile composite specimens using statistical data from micro-computed tomography: 3D tow representations.* Journal of the Mechanics and Physics of Solids, 2012. **60**(8): p. 1561-1581.
15. Yu, B., et al., *Evolution of damage during the fatigue of 3D woven glass-fibre reinforced composites subjected to tension–tension loading observed by time-lapse X-ray tomography.* Composites Part A: Applied Science and Manufacturing, 2016. **82**: p. 279-290.
16. Chiang, C., *Prediction of the fracture toughness of fibrous composites.* Journal of materials Science, 2000. **35**(12): p. 3161-3166.
17. Wells, J. and P. Beaumont, *Fracture energy maps for fibre composites.* Journal of Materials Science, 1982. **17**(2): p. 397-405.
18. *Hexcel HexPly M21, Epoxy Matrix Product Datasheet*.

19. Achanta, R., et al., *SLIC superpixels compared to state-of-the-art superpixel methods.* IEEE transactions on pattern analysis and machine intelligence, 2012. **34**(11): p. 2274-2282.
20. Rother, C., V. Kolmogorov, and A. Blake, *" GrabCut" interactive foreground extraction using iterated graph cuts.* ACM transactions on graphics (TOG), 2004. **23**(3): p. 309-314.
21. Vincent, L., *Morphological area openings and closings for grey-scale images*, in *Shape in Picture*. 1994, Springer. p. 197-208.
22. Pimenta, S., et al., *Mechanical analysis and toughening mechanisms of a multiphase recycled CFRP*. Composites Science and Technology, 2010. **70**(12): p. 1713-1725.
23. Pimenta, S. and S.T. Pinho, *Hierarchical scaling law for the strength of composite fibre bundles.* Journal of the Mechanics and Physics of Solids, 2013. **61**(6): p. 1337-1356.
24. *Hexcel HexTow AS7, Carbon Fibre Product Datasheet*.
25. Bullegas, G., S.T. Pinho, and S. Pimenta, *Engineering the translaminar fracture behaviour of thin-ply composites.* Composites Science and Technology, 2016. **131**: p. 110-122.
26. Greenhalgh, E., *Failure analysis and fractography of polymer composites*. 2009: Elsevier.
27. Katafiasz, T., et al., *The influence of temperature and moisture on the mode I fracture toughness and associated fracture morphology of a highly toughened aerospace CFRP*. Composites Part A: Applied Science and Manufacturing, 2021. **142**: p. 106241.

Appendix

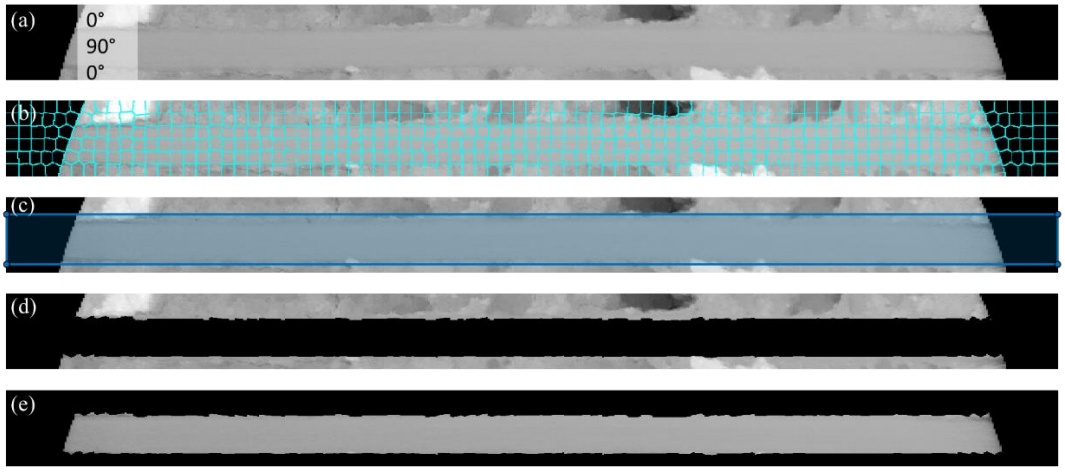

Figure 14: (a) a section of the 2D projection of fracture surface; (b) Superpixels generated after applying Simple Linear Iterative Clustering (SLIC) algorithm [19]; (c) An initial mask defined for the GrabCut algorithm [20]; (d) the segmented 0° plies and (e) the complementary segmented 90° plies.